An integrated approach for prognosis of Remaining Useful Life for composite structures under in-plane compressive fatigue loading

Gül, Ferda C.; Moradi, Morteza; Zarouchas, Dimitrios

DOI
10.1016/j.jcomc.2024.100531

Publication date
2024

Document Version
Final published version

Published in
Composites Part C: Open Access

Citation (APA)
Gül, F. C., Moradi, M., & Zarouchas, D. (2024). An integrated approach for prognosis of Remaining Useful Life for composite structures under in-plane compressive fatigue loading. *Composites Part C: Open Access*, *15*, Article 100531. https://doi.org/10.1016/j.jcomc.2024.100531

Composites Part C: Open Access 15 (2024) 100531

Contents lists available at ScienceDirect

Composites Part C: Open Access

journal homepage: www.sciencedirect.com/journal/composites-part-c-open-access

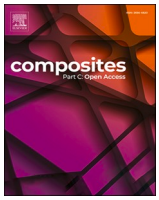

An integrated approach for prognosis of Remaining Useful Life for composite structures under in-plane compressive fatigue loading

Ferda C. Gül *, Morteza Moradi, Dimitrios Zarouchas

Center of Excellence in Artificial Intelligence for Structures, Prognostic and Health Management, Department of Aerospace Structures and Materials, Faculty of Aerospace Engineering, Delft University of Technology, the Netherlands

ARTICLE INFO

Keywords:
Compressive fatigue
Impact damage
Structural Health Monitoring
Guided waves
Remaining Useful Life
Deep learning

ABSTRACT

The prognostic of the Remaining Useful Life (RUL) of composite structures remains a critical challenge as it involves understanding complex degradation behaviors while it is emerging for maintaining the safety and reliability of aerospace structures. As damage accumulation is the primary degradation indicator from the structural integrity point of view, a methodology that enables monitoring the damage mechanisms contributing to the structure's failure may facilitate a reliable and effective RUL prognosis. Therefore, in this study, an integrated methodology has been introduced by targeting the RUL and progressive delamination state via Deep Neural Network (DNN) trained with Guided wave-based damage indicators (GW-DIs). These GW-DIs are obtained via signal processing, Hilbert transform, and Continuous Wavelet Transform. This work uses GW-DIs to train and test the proposed model within two frameworks: one focusing on individual sample analysis to explore path dependency in RUL and delamination prognosis and another on an ensembled dataset to propose a generic model across varying stress scenarios. Results from the study indicate that proposed DNN frameworks are capable of encapsulating fast and slow degradation scenarios to evaluate the RUL prediction with associated delamination progress, which could contribute to ensuring the integrity and longevity of critical life-safe structures.

1. Introduction

Although composite structures are increasingly integrated into aerospace designs due to their high stiffness-to-weight ratio, they are susceptible to specific forms of damage, such as impact damage, that may compromise their load-bearing capacity substantially. Furthermore, when impacted structures are exposed to fatigue loading conditions, these structures undergo complex damage accumulation processes, presenting unique challenges in maintaining airworthiness [1–3]. Ensuring airworthiness, composite structures are subject to life-cycle management procedures based on principles of damage tolerance and safe-life. According to the European Union Aviation Safety Agency's (EASA) acceptable means of compliance (AMC), validating the damage tolerance characteristics of the structure relies critically on detecting and repairing damage before it becomes severe [4]. However, identifying the critical level of the damage severity and foreseeing the remaining time that the structure may reach its threshold level introduce a significant challenge as a result of the inhomogeneous nature of composite structures that create a stochastic degradation phenomenon [5,6].

Among the damage types of composite structures, delamination induced by an impact event carries a severe threat from the structural integrity point of view because of its complex and often hidden nature [7,8]. More specifically, under compressive fatigue conditions, delamination can be particularly concerning due to the resulting reduction in stiffness, which consequently increases the risk of structural buckling [9,10] According to the regulations [4], damage severity assessment must be performed for the structure by determining possible locations, types, and sizes of damage before reaching the critical damage threshold, which enables maintenance actions to be taken at planned inspection intervals. In delamination progress under compressive loading conditions, quantifying delamination severity is complicated as delamination may occur and grow at each layer in different shapes and may present an accelerated growth rate after a critical damage severity level. Moreover, determining the critical damage level is problematic as well, as variations in initial damage besides the operational and environmental conditions may lead to degradation scenarios that differ drastically for each composite structure. As a result, to avoid reaching a critical threshold level, it becomes essential to uncover the delamination growth in

* Corresponding author.
E-mail address: F.C.Gul@tudelft.nl (F.C. Gül).

https://doi.org/10.1016/j.jcomc.2024.100531

Available online 9 November 2024

Nomenclature

CAI	Compression After Impact
CBM	Condition Based Maintenance
CFRP	Carbon Fiber-Reinforced Polymer
CWT	Continuous Wavelet Transform
DAQ	Data Acquisition
DIC	Digital Image Correlation
DIs	Damage Indicators
DWT	Discrete Wavelet Transform
EMI	Electromechanical Impedance
GWs	Guided Waves
HT	Hilbert Transform
LOOCV	Leave-one-out-cross-validation
PZT	Piezoelectric Transducer
RUL	Remaining Useful Life
SHM	Structural Health Monitoring
STFT	Short Time Fourier Transform
WAP	Windowed Avarage Power
N_{cycle}	Number of cycles
N_{path}	Number of paths
N_{DI}	Number of DI
F_{max}	Maximum applied load
F_{min}	Minimum applied load
$\Psi(t)$	Wavelet function
a_m^l	Neuron input
f_{exc}	Excitation frequency
ν	Exponential average of gradients
β	Exponential decay control parameter
g	Gradient
η	Initial learning rate
ω	Weight of a neuron
s	Exponential average of squares of g
x	Damage indicator
$\overline{Y}_d^{i,m}$	True label of delamination length
$\overline{Y}_d^{i,p}$	Predicted value of delamination length
$\overline{Y}_R^{i,m}$	True value of delamination length
$\overline{Y}_R^{i,p}$	Predicted value of delamination length

real-time, and that necessitates the development of sophisticated prognostic models that reveal the delamination state and the RUL of the structure that may enable reliable and effective repair decisions that consequently enhance the safety and operational efficiency of composite structures.

Structural Health Monitoring (SHM) has emerged to ensure the safety and reliability of engineering structures by continuously assessing their condition [11,12]. By various sensing technologies and data analysis methods, SHM systems enable real-time monitoring of structural integrity, early damage detection, and informed decision-making regarding maintenance and repair activities . The prognosis of RUL is considered the final level of SHM as its process involves capturing structures' complex and nonlinear degradation mechanisms, incorporating uncertainties arising from environmental and operational variability [13].

In the literature, RUL prognostics have been studied through a variety of SHM techniques tailored to specific applications, including Acoustic Emission (AE), Fiber Optic Sensors (FBGs), and Ultrasonic Guided Wave/Lamb Wave (GWs), which offer unique capabilities for monitoring structural health and detecting the signs of deterioration. In the study of [14], AE features have been employed as the input of a data-driven prognostic model to predict the RUL of open-hole CFRP specimens subjected to tensile fatigue loading. Strain-based health indicators are obtained via FBGs in the study of [15], and RUL is predicted for CFRP single-stiffened panels using Gaussian Process Regression. In presented RUL prognostic methodologies, models are trained via Health Indicators (HIs), which are damage-sensitive features obtained from SHM data, targetting the RUL, while the direct and interpretable correlation of HIs with different damage types and states of the structure is not clear. However, within the framework of decision-making processes take place in maintenance strategies, damage characterization with damage severity assessment may enhance and support the RUL prognosis.

GW-SHM is one of the strong candidates among various SHM techniques thanks to its strong ability to examine the structure over long distances compared to their wavelength [16] and unique advantages for detecting and characterizing damage in composite materials, including sensitivity to various damage types and the capability to inspect minor damages [17,18]. The presence and evolution of damage can be potentially monitored through changes in the behavior of GWs, such as variations in wave velocity, attenuation, or mode conversion, which may indicate the location, existence and severity of damage [19]. GW signals can be performed through piezoelectric (PZT) transducers with an excitation signal and can be operated in either pitch-catch or pulse-echo strategy in chosen intervals [20,21].

GWs have been employed for damage detection and localization for composite structures, demonstrating notable capabilities in this regard [22]. The research conducted in [23] demonstrates the capability of GW-DIs in classifying damage types via Gaussian discriminant analysis for CFRP coupons subjected to tensile fatigue loading. Efforts to monitor the growth of delamination have been undertaken in study [24] employing GW-DIs with the implementation of the experimental study given in [25]. Nonetheless, it is crucial to extract DIs from GW signals that involve sophisticated advanced signal processing techniques to isolate significant features indicative of underlying structural changes. Hilbert Transform (HT) is a signal processing technique that estimates the signal's envelope through its analytical representation, allowing DI extraction in the time domain [26]. Additionally, given the non-stationery and time-varying nature of GWs, Continuous Wavelet Transform (CWT) holds relevance for the analysis due to its ability to detect localized features that make it well-suited for examining signals characterized by abrupt changes or transient events [27,28]

The relation between the acquired GW-DIs with RUL and the delamination state may present a complex correlation requiring a model to map their interconnection effectively. Besides that, sensors in the same network may present some deviation originating from sensor-based imperfection or uncertainties due to the sensor attachment and the possible effect of the actuator-sensor paths closer to the damaged area. This could lead to variability in GW-DIs, making some more sensitive to delamination growth. At the same time, others may convey information not only about delamination but also about structural variations in a broader sense. Therefore, prediction models that account for complex data patterns and adapt over time are needed for accurate and reliable prognostic output. In the literature, data-driven RUL and damage severity prognostic have been implemented through statistical and machine-learning-based methods [29]. Among these techniques, DNNs are recognized for their capability to effectively capture complex, nonlinear relationships hidden in the data, thereby facilitating the mapping of complex correlations between GW-DIs and damage characteristics [30,31]. Additionally, their capacity to learn from vast and heterogeneous datasets enhances their adaptability to diverse damage scenarios, such as sudden growth behavior observed under compressive fatigue loading conditions [32,33]. However, DNN models face challenges such as model generalization, the risk of overfitting, and the

interpretability of the learned representations, which may limit the comprehension of the underlying physical processes [34,35].

Although various studies have proposed RUL prognostics for composite structures, more research should address the delamination propagation and its correlation with RUL using SHM data in a data-driven methodology. Additionally, while data-driven RUL prognostic models in the existing literature have infrequently utilized GW-SHM data as input, extensive research has been conducted on diagnostics with GWs. Considering the effectiveness of GW-DIs in damage characterization, incorporating these indicators into RUL prognostics offers considerable potential to enhance the precision and dependability of the predictions [36,37]. Moreover, most of these studies mainly focus on structural degradation under tensile fatigue conditions, which presents an area for further investigation to enhance RUL prognostics' predictive accuracy and applicability in composite structures under varied compressive scenarios. Thus, this paper proposes a novel GW-SHM-based integrated prognostic approach that targets RUL and delamination size in a data-driven framework for woven CFRP samples subjected to compressive fatigue loading conditions. In this study, delamination is initiated by a low-velocity impact and is considered as the dominant damage mechanism that leads to the final failure of the samples. The prognostic concept aims to improve the learned representations' interpretability by targeting RUL and delamination size as separate outputs in the learning framework. Through advanced signal processing, GW-DIs are extracted as high-level features from GW signals, aiming for more robust and interpretable prognostic outcomes for RUL and delamination size. A DNN model is implemented in this work as the prognostic model. Model architecture and hypermeters are adapted and tuned according to the input and output sets, focusing on two objectives. The first is to investigate the contribution of various paths to the prognostic of RUL and delamination size in each sample domain. The second objective is to achieve a more generic prognostic model with ensembled GW-DIs from different samples arranged as the DNN model's input set. The proposed methodology enables monitoring the contributing damage mechanisms to failure of the structure that results in a reliable and effective RUL prognosis.

Within the methodology of this study, GW signals are acquired through a surface-bonded PZT network. The damage state is labeled via the ultrasonic C-scan technique, and damage size is quantified as the maximum measured length, which is applied from the industrial application point of view. RUL is determined as the total EoL cycle that occurs due to catastrophic failure in all samples and the last prediction step indicates the critical damage level for each sample. GW-DIs are estimated via HT and CWT, and particular constraints are assigned for each to obtained GW-DIs. Finally, an integrated approach is developed to facilitate RUL and delamination state prognostic.

The rest of the paper is organized as follows: The experimental study that produced the dataset for this work is described in the following section. The third section presents the methodology of GW-based SHM, DI extraction, and DNN-based regression models. The fourth section presents the prognostic framework, introducing the dataset organization and model architecture. In the fifth section, results are presented with their discussion Sections. The last chapter includes the conclusion and future work.

2. Experimental study

2.1. Compression-compression fatigue experiment

Compression After Impact (CAI) fatigue testing has been designed and adapted for samples tailored from a large woven-type CFRP plate according to the ASTM D7136 [38]. Each sample has a thickness of 5.5 mm, with dimensions of 100 mm in width and 150 mm in length. Fig. 1 shows the experimental setup, presenting the impact testing, fatigue testing with SHM setup, and the anti-buckling fixture used in testing to prevent global buckling. The acquisition step of the experiment is

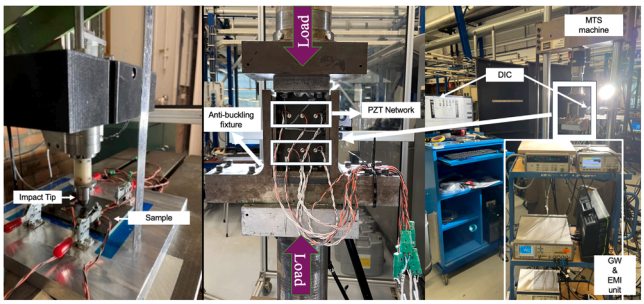

Fig. 1. CAI fatigue testing with SHM setup.

achieved through multiple data acquisition (DAQ) systems: GW, electromechanical impedance (EMI), digital image correlation (DIC), and pulse-echo ultrasonic C-scan. The equipment list in the GW & EMI unit consists of a signal generator, EMI analyzer, multiplexor, oscilloscope, and computer.

In the initial stage of the experiment, data on the undamaged condition of the samples was collected. In the following step, the samples were subjected to low-velocity impacts using a drop-weight, followed by another data collection step to assess their condition post-impact. While healthy state and after-impact state acquisition steps have been done in free boundary conditions, this means the sample was not located inside the fixture, and no in-plane stress was introduced. Cycle 0 indicates the step that data was collected while the samples were clamped with a minimum magnitude of stress applied. In later processing, Cycle 0 was used as a reference

signal to compare fatigue data, as data acquisition was done under the same conditions as Cycle 0 for each sample throughout the fatigue testing.

The fatigue testing begins with an initial slow cycle at 1 Hz, followed by cycles executed at 5 Hz. Throughout the test, a load ratio of 10 is maintained consistently. In the dataset, constant load was applied to five samples: Sample 7, 9, 13, 14, and 15. Sample 2 has experienced constant loading except for its initial slow loading cycle, where the maximum load applied exceeded the defined fatigue force. Sample 10 initially experienced a higher load level before gradually decreasing force over later cycles. Sample 12 was subjected to a lower load level, and its load was gradually increased over the following cycles. Consequently, constant and non-constant fatigue conditions were explored within the dataset, and their details are given in Table 1.

2.2. Delamination state labels

Throughout the tests, ultrasonic C-scan measurements were conducted using a Dolphicam 2. The non- destructive test (NDT) kit (facilitated by the Dolphitech technology) operates on the pulse-echo principle with an excitation center frequency of 8 MHz. It facilitates the reconstruction of delamination images through post- processing in two methods: one involves amplitude variation and the other utilizes time-of-flight information, enabling the acquisition of delamination images throughout the thickness.

Fig. 2 shows the maximum measured length of delamination monitored via C-scan for Sample 7. As seen in the figure, a one-dimensional quantification method is employed in this study as the maximum length of the delamination growth that occurs perpendicular to the direction of the applied load. An equal final length is defined for the EoL of all the samples, with the evidence of delamination reaching both edges of the sample in the growth direction, which is limited by the width of the sample. Among the samples in the dataset, Sample 12 and Sample 13 are two samples whose damage state was not able to be labeled via C-scan because of the high-noise effect in the images; thus, these two samples were not involved in the prognostic models that target delamination length as the output. Fig. 3 represents the dataset showing the

Table 1
Test parameters and results of samples assigned in proposed methodology.

Samples	Impact Energy (Joule)	Max/Min Force	Max Applied Force	EoL (Cycles)	Samples	Impact Energy (Joule)	Max/Min Force	Max Applied Force	EoL (Cycles)
Sample 2	19.45	$\frac{-135kN}{-13.5kN}$	−140 kN	79,000	Sample 12	19.45	$\frac{-130kN}{-13kN}$	−137 kN	38,500
Sample 7	15.35	$\frac{-140kN}{-14kN}$	−140 kN	40,500	Sample 13	16.31	$\frac{-140kN}{-14kN}$	−140 kN	27,900
Sample 9	15.35	$\frac{-140kN}{-140kN}$	−140 kN	97,000	Sample 14	15.35	$\frac{-140kN}{-140kN}$	−140 kN	21,300
Sample 10	15.35	$\frac{-135kN}{-13.5kN}$	−150 kN	6600	Sample 15	16.31	$\frac{-135kN}{-13.5kN}$	−135 kN	15,500

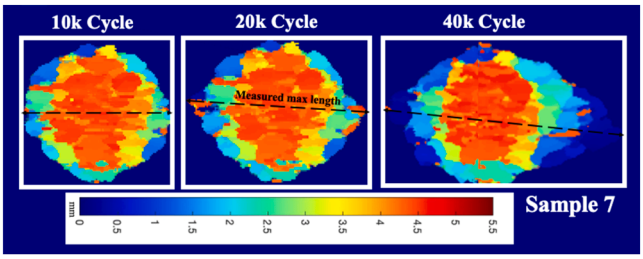

Fig. 2. Delamination length measurement via C-scan images.

measured maximum delamination length of the samples during their fatigue life, corresponding RULs, assigned threshold, and all samples' measured delamination in their threshold. The term "threshold" level, given in Fig. 3, occurs in the cycle step that is followed by a fast delamination propagation, resulting in final failure. Therefore, it indicates the last cycle step that allows for data acquisition and the damage length measurement. The threshold level is measured as a different value for each sample, and it is attributed as the critical damage length for the tested samples.

3. Methodology

This section elaborates on the GW-SHM methodology, initially detailing the experimental parameters essential for collecting GW signals. In the second Section, DIs obtained from GW signals are introduced. In the final sub-section, a prognostic model that is trained with GW-DIs is described. The general methodological framework is given in Fig. 4.

3.1. GW-SHM

GWs are elastic waves propagating within plate-like structures, comprising longitudinal modes, shear modes, and higher-order combinations. Their dispersive characteristics are influenced by structural geometry, ply fiber direction, initial wave entry angle, the excitation signal and frequency chosen [39]. The excitation signal and frequency are essential parameters for GWs. They can activate wave modes,

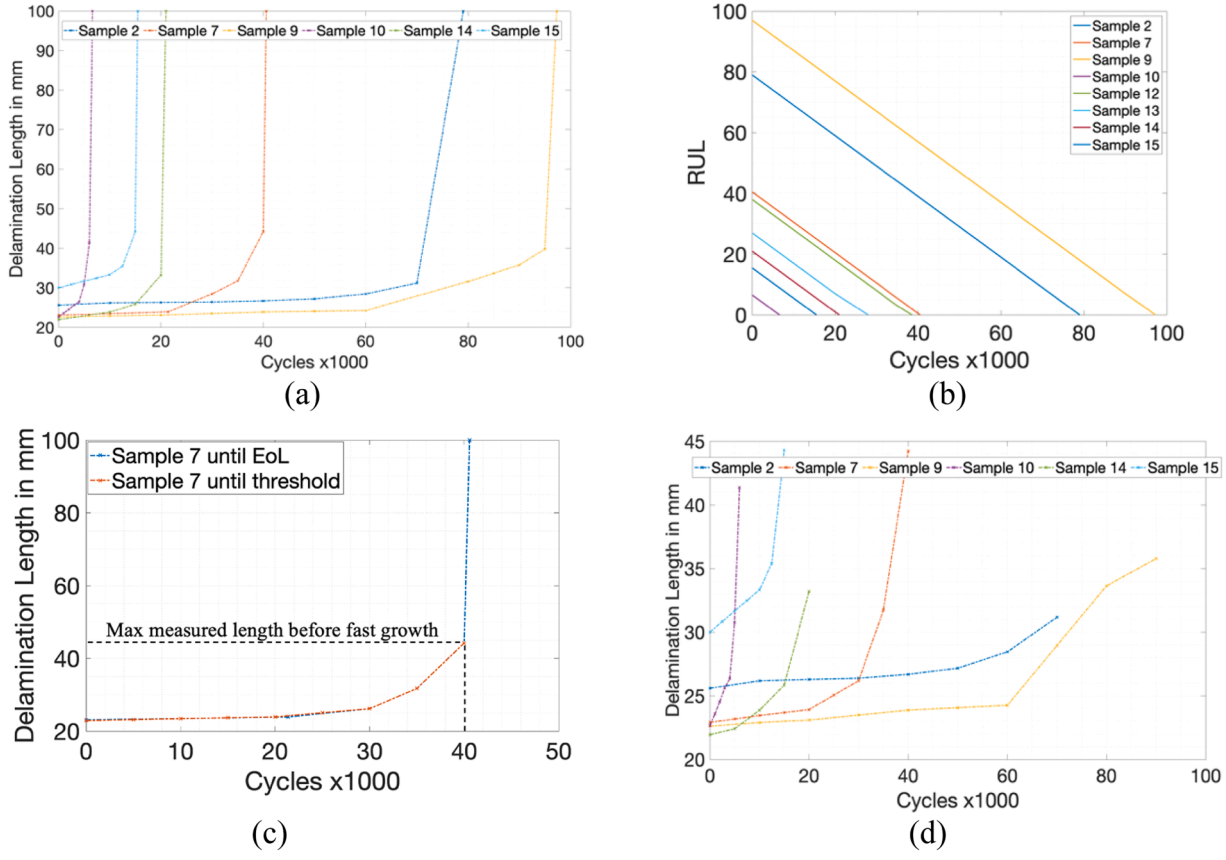

Fig. 3. (. a) Delamination growth until EoL, (b) RUL, (c) Damage threshold, (d) Delamination growth until the threshold level.

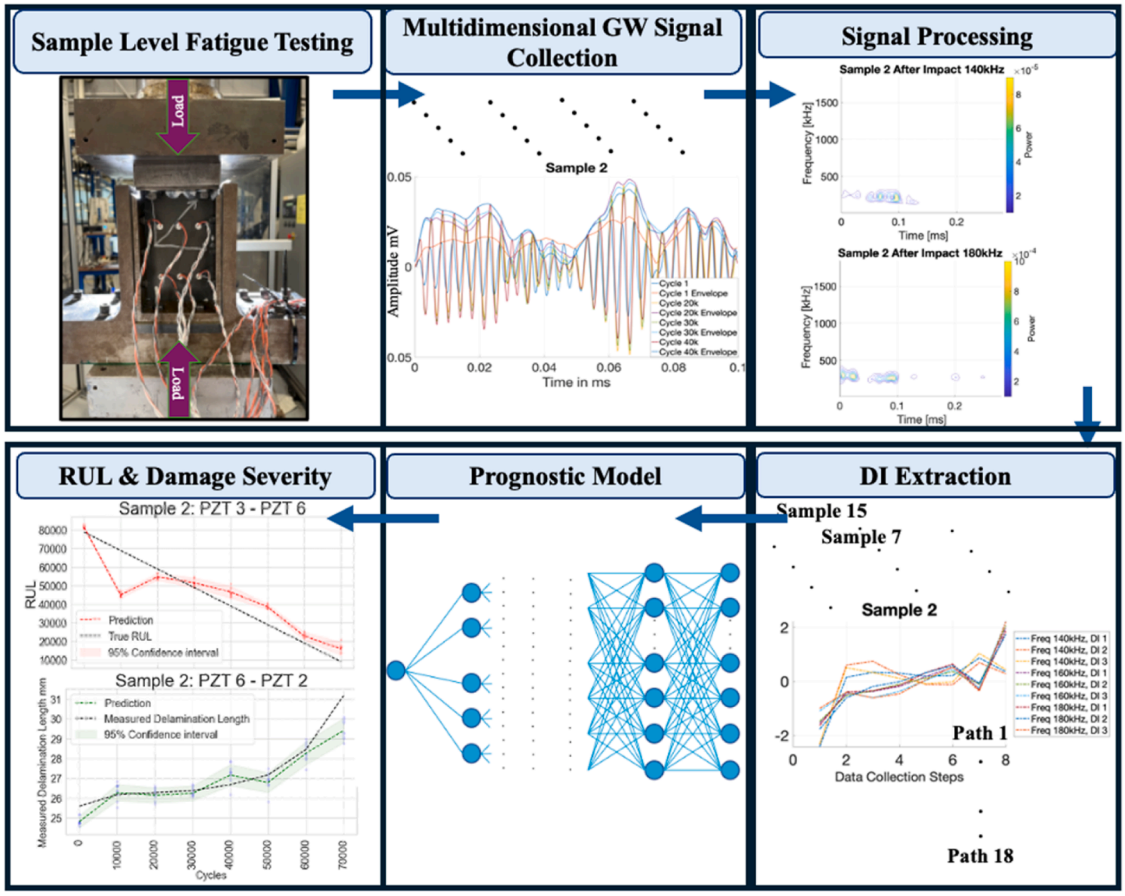

Fig. 4. General GW-SHM based prognostic framework.

including higher modes, which can provide enhanced resolution but may also lead to more complex signal interpretation due to mode conversion and dispersion [20,40,41]. Therefore, they must be optimized according to the structural parameters and damage sensitivity, considering the structure's anisotropy and heterogeneity. However, it is challenging to induce desired GW modes, especially for composites, due to their anisotropic nature. GW signals generated by a 2-cycle tone-burst signal with center frequencies of 140 kHz, 160 kHz, and 180 kHz are utilized in this work to expand the possibility of achieving better signal-damage interaction evident in the acquired GW signal.

GW signals are collected using the pitch-catch mode, wherein each PZT alternates between acting as an actuator and a sensor [42]. Specifically, during data collection, the top array PZTs function as actuators while the bottom array serves as receivers, and vice versa. This setup results in each PZT having three distinct paths, yielding a total of 18 paths collected. Fig. 5 illustrates the labels for each actuator-sensor pair considered in the pre/post-processing and DI extraction step.

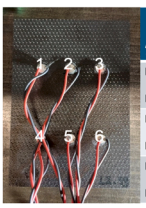

PZT Pair Actuator - Sensor	Path No	PZT Pair Actuator - Sensor	Path No	PZT Pair Actuator - Sensor	Path No	PZT Pair Actuator - Sensor	Path No	PZT Pair Actuator - Sensor	Path No	PZT Pair Actuator - Sensor	Path No
PZT 1 - PZT 4	1	PZT 2 - PZT 4	4	PZT 3 - PZT 4	7	PZT 4 - PZT 1	10	PZT 5 - PZT 1	13	PZT 6 - PZT 1	16
PZT 1 - PZT 5	2	PZT2 - PZT 5	5	PZT 3 - PZT 5	8	PZT 4 - PZT 2	11	PZT 5 - PZT 2	14	PZT 6 - PZT 2	17
PZT 1 - PZT 6	3	PZT 2 - PZT 6	6	PZT 3 - PZT 6	9	PZT 4 - PZT 3	12	PZT 5 - PZT 3	15	PZT 6 - PZT 3	18

Fig. 5. Surface-attached PZT network and actuator-sensor path labels.

3.2. GW-DIs

GW-DIs are obtained through signal processing techniques to identify portions of the GW signal that are particularly sensitive to delamination. Table 2 represents the DI definitions with their corresponding reference equation. GW-DIs are extracted in both the time domain through HT to obtain signal envelope from the analytical presentation of the signal and in the time-frequency domain via the CWT method [43]. In CWT analyses, wavelets, which are localized functions or waveforms, are employed to analyze different signal segments at various scales [44]. The wavelet function is denoted as Ψ(t), and the continuous CWT coefficients as CWT(a,b) . When a signal segment matches the form or pattern of the wavelet, the resulting wavelet coefficients reach their maximum value. The Morlet function has been utilized as the wavelet in this particular CWT analysis. The Morlet function consists of a sinusoidal

Table 2
GWs processing reference equations and damage indicators.

	Reference Equation	Damage Indicator
Hilbert Transform	$H(t) = \frac{1}{\pi}\int_{-\infty}^{+\infty}\frac{x(\tau)}{t-\tau}d\tau z(t) = x(t) + iH(t)$	$DI1_{f_{exc},N_{PZT}} = \frac{\sum_t^{T_{window}} H(t)_{cycles}}{\sum_t^{T_{window}} H(t)_{base}}$
Continuous Wavelet Transform	$CWT(a,b) = \int \psi\left(\frac{t-b}{a}\right) x(t)dt WAP(t) = \sum_{b=t}^{b=T} \lvert CWT(a,b)\rvert$	$DI\ 2_{f_{exc},N_{PZT}} = \frac{\sum_t^{T_{window}} AP(t)_{cycles}}{\sum_t^{T_{window}} AP(t)_{base}}$ $DI\ 3_{f_{exc},N_{PZT}} = \frac{\sum_t^{Ttotal} AP(t)_{cycles}}{\sum_t^{Ttotal} AP(t)_{base}}$

wave enveloped by a Gaussian and closely resembles the form of a tone burst signal. Due to this resemblance in waveform shape, the Morlet wavelet is more effective at matching the characteristics of the tone burst signal compared to other types of wavelets, which consequently may result in improved signal decomposition and analysis, allowing for the essential features of the signal to be captured with minimal distortion [45].

A mode-independent approach is conducted in this work with the motivation to derive the information that can be obtained from the rest of the GW signal, potentially from mixed and higher GW modes. In that sense, three DIs have been adopted in this work, which have been studied for delamination progress analysis for the samples tested in the experiment.

For DI 1, a time window is applied to the residual GW signal in the time domain in the ranges of 0–4 μ for 140 kHz, 0–3.5 μ for 160 kHz, and 0–3 μ for 180 kHz, resulting in a longer time window for 140 kHz lower frequency of and a shorter one for 180 kHz. Owing to this approach, initially arrived energy packages are captured; thereby, the effects of reflections are mitigated.

For the second DI, time windows are designated in the time-frequency domain. These windows are centered around the wave package with the highest energy in residual signal, aiming to isolate the portion of the signal most sensitive to damage.

Finally, the entire spectrum is quantified as the third DI in the time-frequency domain, providing a comprehensive overview of the signal's characteristics.

As each f_{exc} frequency contains 3-DIs, the feature extraction step results in 9-DIs to investigate each sample at the end. Fig. 6 presents the DIs of the same path for each sample in the dataset. It can be seen in the figure that not all the DIs have the same characteristics as each other even when they belong to the same sample. As the degradation is a continuously increasing phenomenon, when no repair/replacement takes place, DIs are expected to be monotonic with a similar trend. It can be seen in Fig. 6 that DIs from the same actuator-sensor pair display variation. At the same time, their damaged progress representation may be shadowed by noise, and reflections occur in the signal. While some paths present errors by showing a decreased trend, such as in Sample 10, damage severity indicated by the DIs for the same sample may differ as well. GW signals may not carry only delamination-related information but also information from the entire structure, which may include other types of damage, such as matrix cracks. Thus, although some DIs from the same path may exhibit higher sensitivity to delamination, others with severe DIs may indicate structural degradation from a broader point of view, conveying effects induced by other damage modes as well. Additionally, the variation between the DIs induced by different excitation frequencies may indicate that more delamination-sensitive modes might be excited at those signals that generate more monotonic DIs.

Furthermore, there might be higher-mode excitation due to scattering originating from delamination, yet understanding the complex interplay of factors influencing GW signals is highly challenging. Through the selected signal processing steps, while the delamination-related part of the signal might be better captured for specific frequencies and paths, others might overlook this information. On the other hand, using multiple excitation frequencies and DIs could enhance this hurdle by enabling information fusion for a better prognosis. Moreover, considering that the delamination is the major yet not the only effect that stimulates degradation of the structure, it is likely effective to fuse those DIs for more accurate prognostic that are comprehensive for both the structural degradation and delamination specifically.

3.3. Deep neural networks

DNNs have emerged as powerful tools for regression tasks because they can model complex relationships between input and output variables. Unlike traditional regression methods, DNNs can automatically learn hierarchical representations from data, and they are well-suited for tasks with high-dimensional inputs and nonlinear relationships. The basic building blocks of a DNN are neurons, organized into layers. In a typical DNN architecture for regression, multiple hidden layers are interleaved between the input and output layers. Fig. 7 represents the learning scheme for neuron I in hidden layer l. The term a_m^l

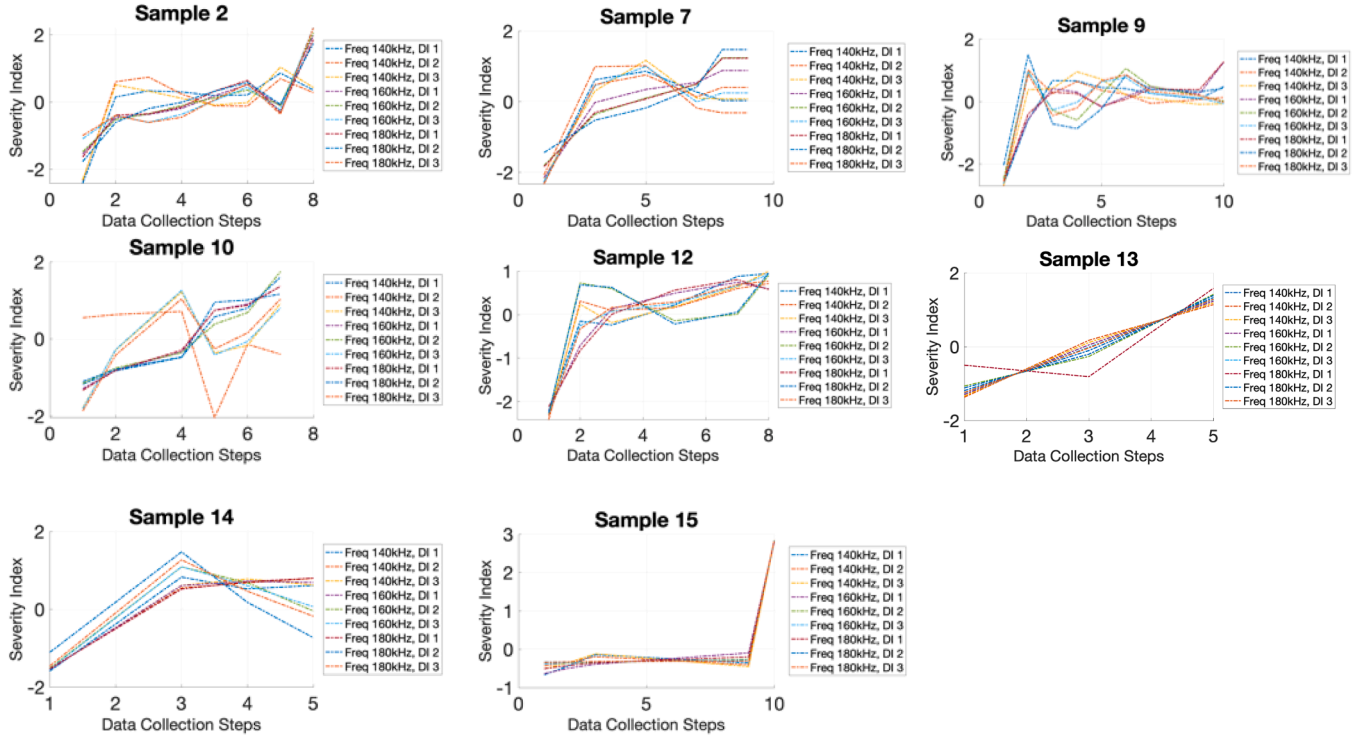

Fig. 6. GW-DIs for path no 5.

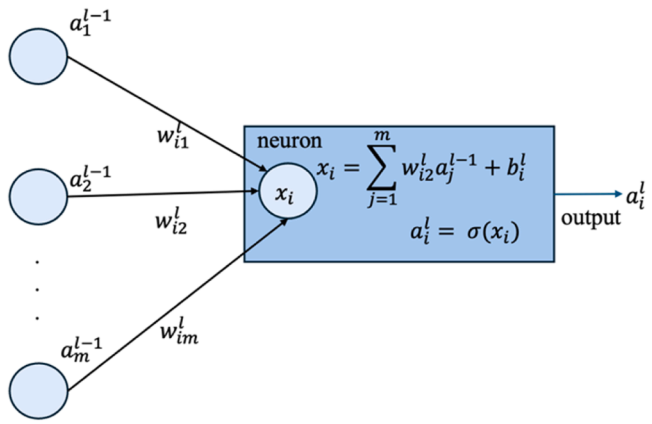

Fig. 7. Neuron input-output relation.

demonstrates the input that arrives from connected neurons of the previous layer while m is the number of neurons and w stands for the weight with bias term b. The term σ is the activation function, which can be either linear or nonlinear, that enables DNNs to capture complex patterns in the data. Commonly used activation functions include the rectified linear unit (ReLU), sigmoid, and hyperbolic tangent (tanh) [46]. Upon experimenting with various activation functions to map DI sets, ReLU and tanh are mainly used in the proposed model due to their effectiveness in producing output with higher accuracy.

Training a DNN for regression involves adjusting the weights and biases of the neurons to minimize a loss function that quantifies the difference between the predicted outputs and the labels. This is typically done using optimization algorithms such as stochastic gradient descent (SGD) or its variants. One of them is Adam, an adaptive optimization algorithm that maintains two moving averages of the gradients [47]. By adapting the learning rates for different parameters based on their historical gradients, Adam often converges faster and is more robust to noisy gradients than traditional SGD methods . Mean squared error (MSE) has been chosen as the loss function and accuracy metric during the training and testing. The Adam's optimization strategy is given in the following equations:

$$\nu_t = \beta_1 * \nu_{t-1} - (1-\beta_1) * g_t \tag{1}$$

$$s_t = \beta_2 * s_{t-1} - (1-\beta_2) * g_t^2 \tag{2}$$

$$\Delta\omega = -\eta \frac{\nu_t}{\sqrt{s_t + \varepsilon}} * g_t \tag{3}$$

$$\omega_{t+1} = \omega_t + \Delta\omega_t \tag{4}$$

where η is the initial learning rate, g_t is the gradient at t each feedfroward iteration along ω_t, ν_t is the exponential average of gradients along ω_t, s_t is the exponential average of squares of gradients along ω_t and β_1,β_2 are hyperparameters to control the exponential decay rates of the moving averages. In addition, among various regularization techniques can be applied to DNNs for regression to prevent overfitting and encourage them to learn more robust representations, dropout layers are assigned to the proposed model as the regularization technique to enhance the model in the sense of its generalization capability [48].

Table 3 presents the hyperparameters of DNN models trained for each framework proposed in this study.

4. Prognostic framework

4.1. Input organization

GW-DIs were extracted for each of the ten samples, resulting in 10 samples x 9; for instance, considering Sample 2, there are 9 DIs collected across 18 paths and eight cycle steps. However, it is essential to note that the number of total cycle intervals that GWs are collected varies for each sample due to the differences in their end-of-life spans, which range from 6600 to 97,000 cycles. At the same time, the data acquisition steps are determined prior to the fatigue test; according to the delamination propagation in the first 1000th and 10,000th cycle, it is re-defined accordingly. To create data steps with constant intervals for each sample, missing values are filled by interpolation after the DI extraction step for samples 7, 10, 12, and 15.

As two different approaches have been investigated for the prognosis of delamination growth and RUL in this work, the datasets are organized in two ways. For the first dataset type, data has been prepared for training considering the model's input size equals the number of DIs, N_{DIs}, and the number of frequencies, N_f. Paths are divided into two groups for training and testing purposes. For each sample, a total of 18 paths have been separated in terms of the actuator-sensor path, resulting in 15 paths for training and three paths for testing considering leave-one-out-cross-validation (LOOCV) that allows for the evaluation of the model's performance using data that was not previously introduced during training, thereby assessing their effectiveness in handling unseen data. More detail, paths from five actuators to each three sensors are assigned to the training set, while one actuator to three sensor paths are reserved for the testing set. This arrangement facilitates a comprehensive evaluation of the performance of DIs based on specific testing paths. Outputs are quantified delamination length and RUL with a threshold that is indicated individually for ten samples, except Sample 12 and Sample 13, as they do not have an accurate damage quantification; therefore, their output is only defined as y_{RUL}.

The dataset has been organized for Framework 2 so that the training set contains DIs from each sample, and the number of neurons in the input layer was allocated considering the number of paths in addition to N_f and N_{DI}. This approach results in a total neuron number of $9 \times 18 = 162$ in the input layer. While the data organization remains the same, RUL and delamination length prediction models used different sample sets; for the RUL prediction, Sample 2, Sample 7, Sample 9, Sample 13, Sample 14, and Sample 15 are merged considering the prognosability, which means the distribution of samples end-of-life merit. Conversely, for the delamination length prediction, Sample 2, Sample 7, Sample 9, Sample 10, Sample 14, and Sample 15 pooled, as Sample 12 and 13 have no complete damage state labels.

The final steps in the data organization procedure for Frameworks 1 and 2 involve normalization and standardization, which are crucial for enabling the model to learn effectively, leading to better generalization and improved performance when making predictions on new data. Normalization involves scaling the data to a range between 0 and 1, ensuring consistency and preventing any feature dominating the model's learning process. This is particularly useful when dealing with features of varying magnitudes, ensuring each feature contributes

Table 3
Hyperparameters of the DNN model.

Type		Number of Neurons										Initial Learning Rate	Batch Size
		L 1	Act. Func.	L 2	Act. Func.	L 3	Act. Func.	L 4	Act. Func.	L 5	Act. Func.		
1		240	ReLU	120	ReLU	60	ReLU	30	ReLU	1	Linear	0.0001	L_c^s
2	A	240	ReLU	120	ReLU	60	ReLU	30	ReLU	1	Linear	0.001	4
	B	240	tanh	120	tanh	60	ReLU	30	ReLU	1	Linear	0.001	4

proportionally to the model's training. For framework 1, the input data in the sample domain considers each path independently for a 0 to 1 normalization. Standardization involves transforming the data to have a mean of 0 and a standard deviation of 1. This process ensures that the features are centered around zero and have a consistent scale, making it easier for the model to converge during training. Framework 2 uses the standardized dataset, considering each specific path of each sample separately to ensure that varying magnitudes are retained to maintain the uniqueness of each data point in the input set. Any data leakage is prevented as the training and testing data are standardized in their own domain.

4.2. Model architectures

The DNN model has five layers for regression tasks, with the last layer having one output for each learning phase, RUL and damage length. The complete learning scheme is illustrated in Fig. 8. In the case of Framework 1, the DNN model is re-trained for both RUL and damage length targets each time the training-testing sets are shuffled, and this process is repeated such that each path in the dataset is used once as the test set. In this framework, training and testing are achieved in the one-sample domain. The path sensitivity is investigated as each actuator-sensor path is involved/excluded one after another, and the same procedure is repeated for each sample in the dataset in LOOCV manner. In the second framework, multiple samples are collected in training, and one sample not included in the training is used in the testing phase following the LOOCV as well.

Hyperparameters are optimized experimentally by surveying the training loss in terms of the MSE value, and they are chosen once the model becomes stable and has the highest accuracy. Table 2 gives the hyperparameter values that are tuned for each framework. For type 1, batch size L_c^s denotes the max value of N_{cycle} for each sample and takes the values of 8, 9, 10, 5, 5, 8, 6, 5, 10 in the training phase of the corresponding sample. The model characteristics were applied in the same way for the RUL target and delamination length. In type 2, the model has two sub-types; type A is trained according to the target of delamination length, and type B is tuned for RUL prediction. For both types, batch sizes remain constant, and the activation function is adapted as tanh for the first two layers' outputs, while type A has ReLU as its activation function. Dropout regularization layers are used after layer 1 and layer 2 with a value of 0.2. Finally, to generate confidence bounds for the predictions, the model was re-initiated and re-trained ten times with different initial weights, yielding varied predictions each time. This approach demonstrated the stability of the proposed model by illustrating how predictions consistently fell within a specific range, confirming the robustness of the model across initializations.

5. Results

5.1. Framework 1

5.1.1. Prediction results

This section presents and discusses prediction results according to Framework 1. As the model is re-trained separately for each output set of delamination length and RUL, the performance of each path from each sample is investigated in a comparative way for the samples shared between damage size and RUL prediction training stack. Errors of predictions are given by the metric of Mean Absolute Relative Error (MARE) [49], given in equation 1, while $\overline{Y}_d^{i,m}$ denotes the true label for delamination length, $\overline{Y}_R^{i,m}$ is the true label for RUL. $\overline{Y}_d^{i,p}$ refers the predicted delamination length at ith cycle and $\overline{Y}_R^{i,p}$ is for the predicted value of RUL. In Fig. 9, errors based on MARE is presented for each path for delamination length prediction. In contrast, the correct figure presents the average error of each path per cycle. The figure indicates error values for RUL prediction based on each testing path and the path average error per cycle. According to the obtained error values, it is evident that paths with higher accuracy vary for each sample.

Furthermore, less effective paths in predicting delamination length may not necessarily yield poor outcomes for RUL prediction. However, a correlation can be captured in the case of Sample 7, Sample 14, and Sample 15, where the lowest MARE for delamination length prediction exhibits high accuracy in RUL prediction. In the case of Sample 7, path 8 has a high prediction error for delamination length prediction, and it holds the same behavior for RUL prediction as well. As the predictions are GW-DIs based, this correlation can be considered as the sensitivity of these DIs to delamination.

Another aspect requiring attention in the error values given in Fig. 9 is that the errors for RUL prediction appear to be generally higher than delamination length prediction. This can be attributed to the nature of the RUL target values, which typically have a higher range, often in the order of 10,000 cycles. In contrast, delamination length targets exhibit smaller intervals; for instance, Sample 2 indicates a prediction range of 25 to 33.6 mm. Consequently, if the model incorrectly predicts the final cycle, for example, estimating 30,000 instead of 1000, the resulting error is significantly amplified, overshadowing the accuracy of predictions made for earlier cycles, which is apparent in Fig. 9 in cycle-based results, in Figure b and d..

$$MARE_{path_d} = \frac{1}{N_{cycle}} \sum_{i=1}^{N_{cycle}} \left| \frac{\overline{Y}_d^{i,m} - \overline{Y}_d^{i,p}}{\overline{Y}_d^{i,m}} \right|, \quad MARE_{cycle\_d} = \frac{1}{N_{path}} \sum_{i=1}^{N_{path}} \left| \frac{\overline{Y}_d^{i,m} - \overline{Y}_d^{i,p}}{\overline{Y}_d^{i,m}} \right| \tag{5}$$

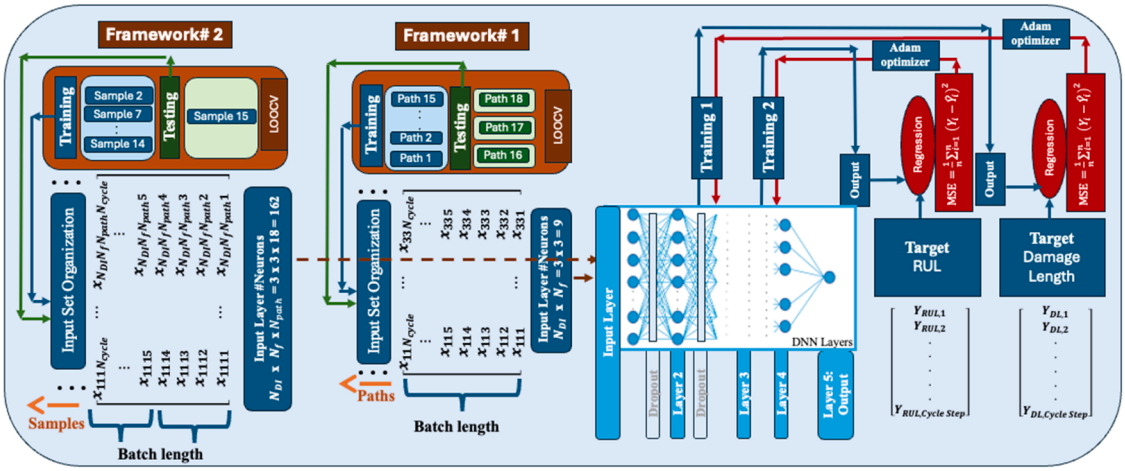

Fig. 8. Representation of learning frameworks.

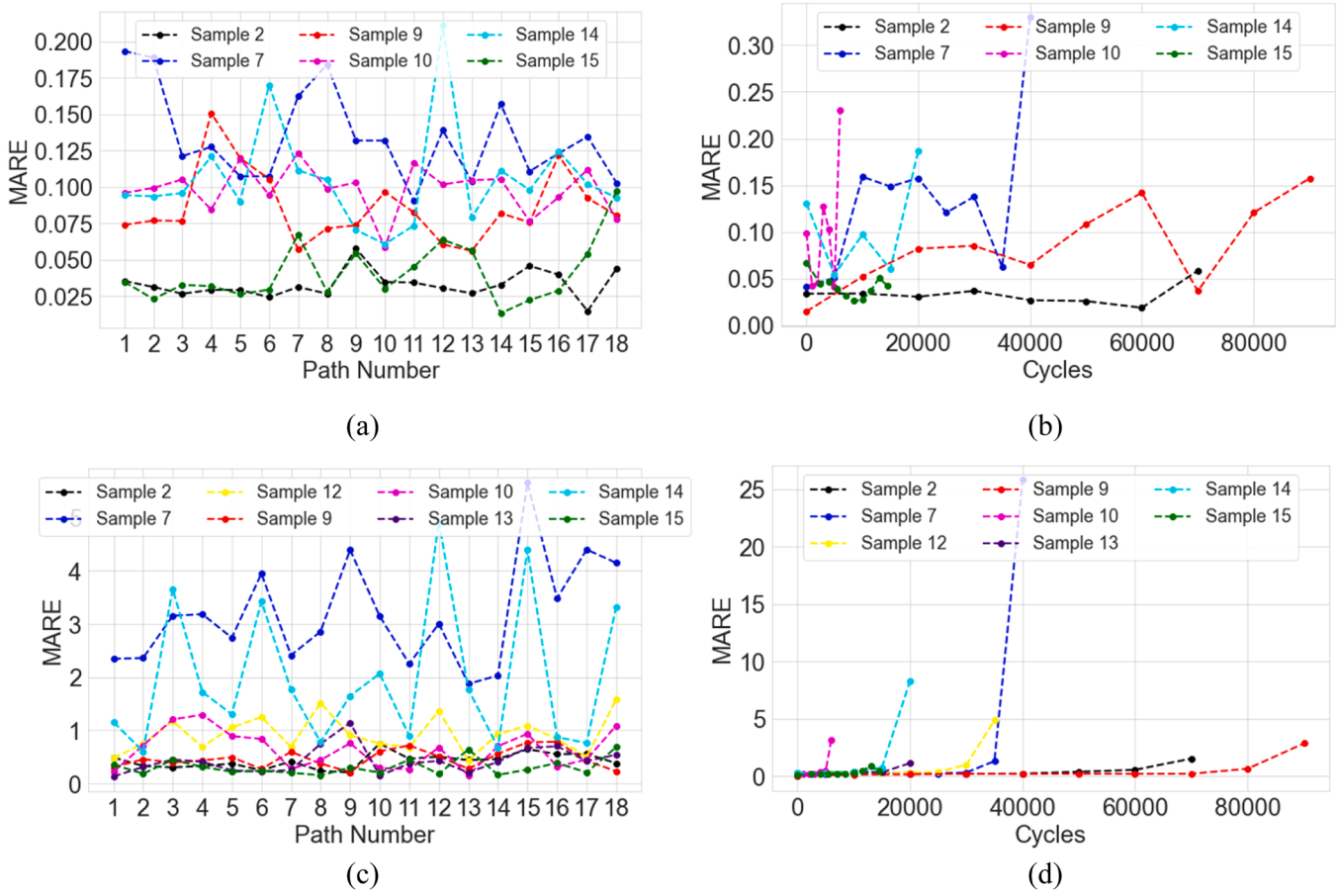

Fig. 9. Error values for (a) delamination length prediction of each path (b) each cycle and for c) RUL prediction of each path d) each cycle.

$$MARE_{path_R} = \frac{1}{N_{cycle}} \sum_{i=1}^{N_{cycle}} \left| \frac{\overline{Y}_R^{i,m} - \overline{Y}_R^{i,p}}{\overline{Y}_R^{i,m}} \right|, \quad MARE_{cycle\_R} = \frac{1}{N_{path}} \sum_{i=1}^{N_{path}} \left| \frac{\overline{Y}_R^{i,m} - \overline{Y}_R^{i,p}}{\overline{Y}_R^{i,m}} \right| \tag{6}$$

According to Fig. 9, cycle-based error representation, both figures reveal that model predictions exhibit lower accuracy for the latest cycle step across all RUL and delamination length prediction samples, except for Sample 15, where the lowest accuracy occurs one step before the final cycle step. Conversely, predictions for damage length still exhibit some error, although not as pronounced as for the final cycle step; the error is likely distributed across each cycle step. In contrast, RUL predictions show a more drastic variation in accuracy, with significant decreases observed for the final cycle step compared to earlier cycles. To investigate the results better, DIs' sensitivity to delamination accumulation should be considered. In contrast to the others, in terms of the delamination in the threshold level, the less sensitive paths might have less confidence and accuracy, which may bring higher errors in the results for the final step prediction. This lower accuracy at the threshold level for specific paths might result from high scattering and reflection in the signal induced by larger delamination.

To compare the performance of testing paths on each trained model, the path with the highest accuracy for delamination length prediction is selected for each sample. Subsequently, the results of the same path for RUL and delamination length prediction are presented together in Fig. 10. In Fig. 11, on the other hand, the paths with the highest accuracy for RUL predictions are selected, and their performance is also demonstrated for delamination length predictions together. The figures indicate that paths performing well on delamination prediction yield RUL prediction almost as good as delamination length prediction. Samples 10 and 15 exhibit considerably good accuracy for both targets in terms of their convergence in the final cycle. In the context of delamination length prediction, the target presents a significant increase in the later cycles. Although the model can generally capture this trend in most samples, it tends to underestimate the maximum delamination length, and this underestimation becomes the primary source of average error.

Besides, it should be highlighted that, even if the accuracy is lower in final cycles, the coherence between the delamination and RUL predictions is visible. In the case of Sample 2, as the model predicts that delamination is growing, the RUL prediction at the same cycle step is decreasing, indicating severe damage accumulation. This pattern is observed in almost all samples, demonstrating the reliability and consistency of the model and the input DI data. However, it may not accurately reflect the actual conditions in every case.

Moreover, when comparing Figs. 10 and 11, it becomes evident that while paths yielding the best predictions for delamination length still maintain acceptable accuracy for RUL prediction, the opposite is not valid for all the samples. Paths resulting in the highest accuracy for RUL prediction do not exhibit the same level of performance for delamination length predictions for all samples. For example, Sample 9, apart from the lower accuracy, the confidence bounds are also larger, indicating lower confidence in the predictions for delamination length for the path produce most accurate RUL prediction.

5.1.2. Discussion

Prediction results based on a one-sample-domain have been presented in this section by investigating each path's contribution to RUL and delamination length prediction. As mentioned in the previous section, for some samples, while the predictions both perform well for delamination prediction and RUL prediction, some may exhibit differently from each other. To understand the underlying reasons for this

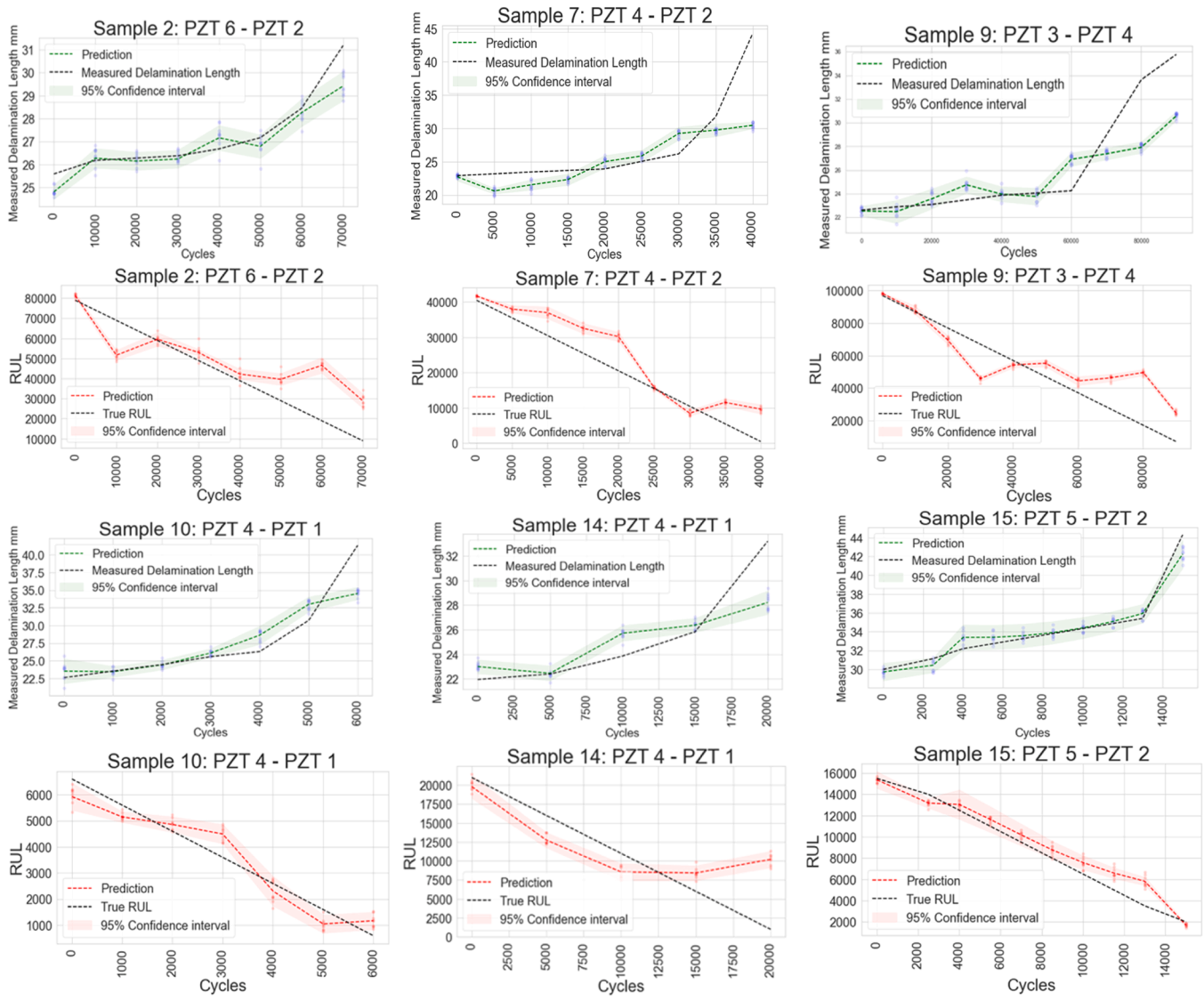

Fig. 10. Comparison of the best results of delamination length prediction with the RUL predictions of the same path.

discrepancy, it is important to discuss possible factors that may contribute to these results.

Firstly, the focus can be given to DIs and the information in which they excel. DI extraction step was carried out specifically to isolate the delamination-related portion of the GW signal, which enables the investigation of the contribution of delamination growth to the end-of-life of the samples. This is a challenging task to achieve, and for some DIs, delamination information might be limited, or information from other damage types might co-exist. Hence, it would be logical to observe that paths that are more sensitive to delamination growth result in higher accuracy in predicting maximum delamination length and still perform well on RUL prediction. On the other hand, paths demonstrating higher accuracy in RUL prediction are likely to encapsulate information from the entire structure, potentially encompassing other types of damage that contribute to the assessment of delamination propagation, and these paths may operate not only for delamination but still play a role in determining the overall health state of the sample.

As mentioned earlier, the primary source of error in many predictions lies in the final prediction step. For instance, in the case of Sample 7, the model's overall performance is not poor; however, it exhibits moderate accuracy until the 35000th cycle high error occurs at the final cycle step. The issue arises from the faster growth of delamination length, measured at its maximum length, a trend that the model failed to capture from the data indicating a potential difference in the input DIs and their ability to reflect damage evaluation for each sample.

5.2. *Framework 2*

5.2.1. *Prediction results*

In this section, the second framework proposed in this work is presented. In Framework 2, the training set is determined in combination with multiple samples and paths tested in Framework 1 and assigned as features aiming that the model will capture the information most relevant to the targeted output. This model has two sub- types to obtain the most accurate and stable model for each target. Subtype A targets the delamination length values as output, and subtype B is trained using the RUL target. Chosen samples to be merged for LOOCV folds are created differently for both sub-types. The delamination length prediction model is trained based on Sample 2, Sample 7, Sample 9, Sample 10, Sample 14, and Sample 15. The RUL model is constructed based on Sample 2, Sample 7, Sample 9, Sample 12, Sample 13, Sample 14, and Sample 15, considering their closer prognosability.

Fig. 12 presents prediction results based on the delamination length prediction. Among the results, the best convergence is observed for Sample 7, while poor coherence is evident for Sample 2 and Sample 10. Sample 9 gradually performs better after the 50000th cycle. Despite the

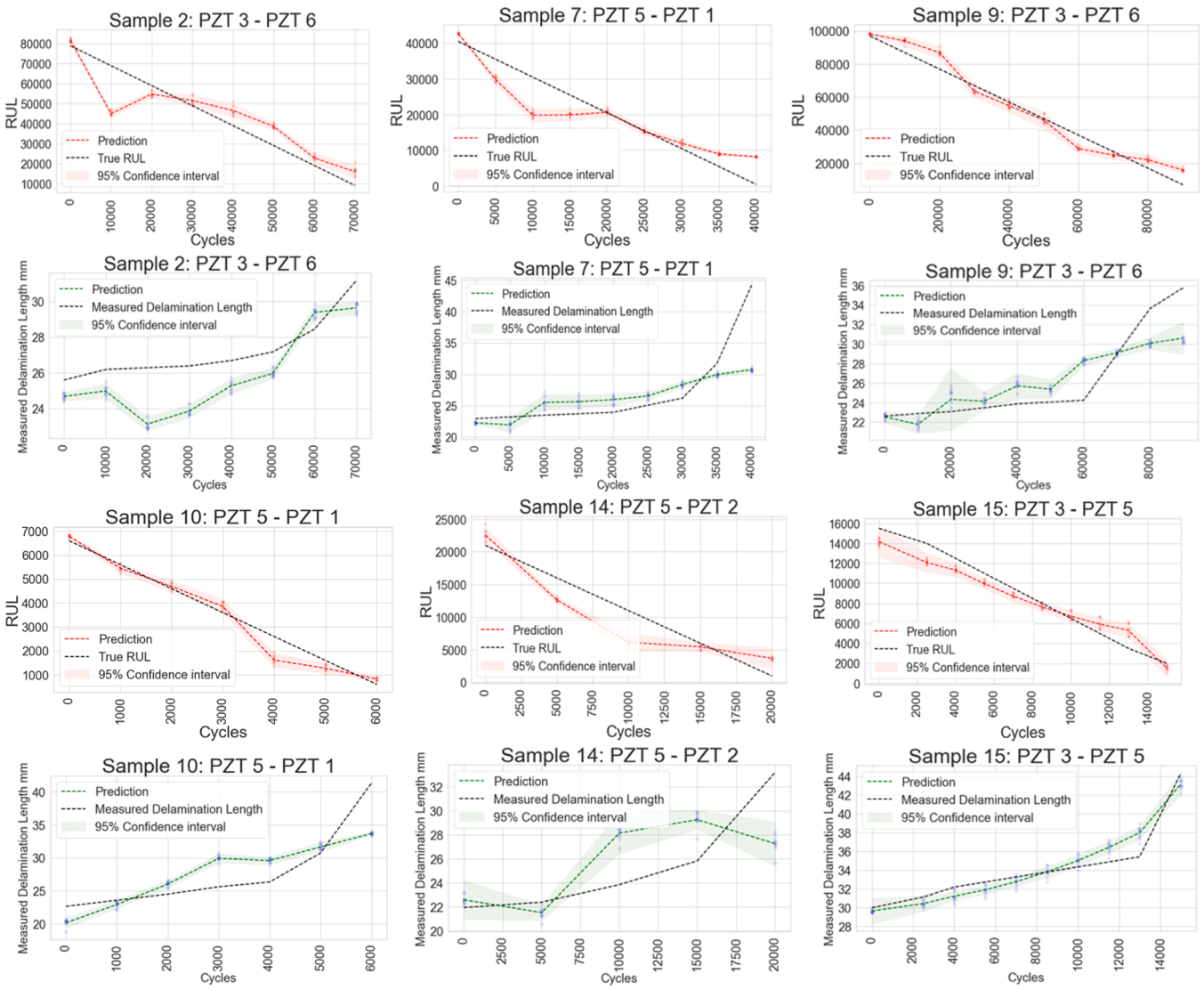

Fig. 11. Comparison of the best results of RUL prediction with the delamination length predictions of the same path.

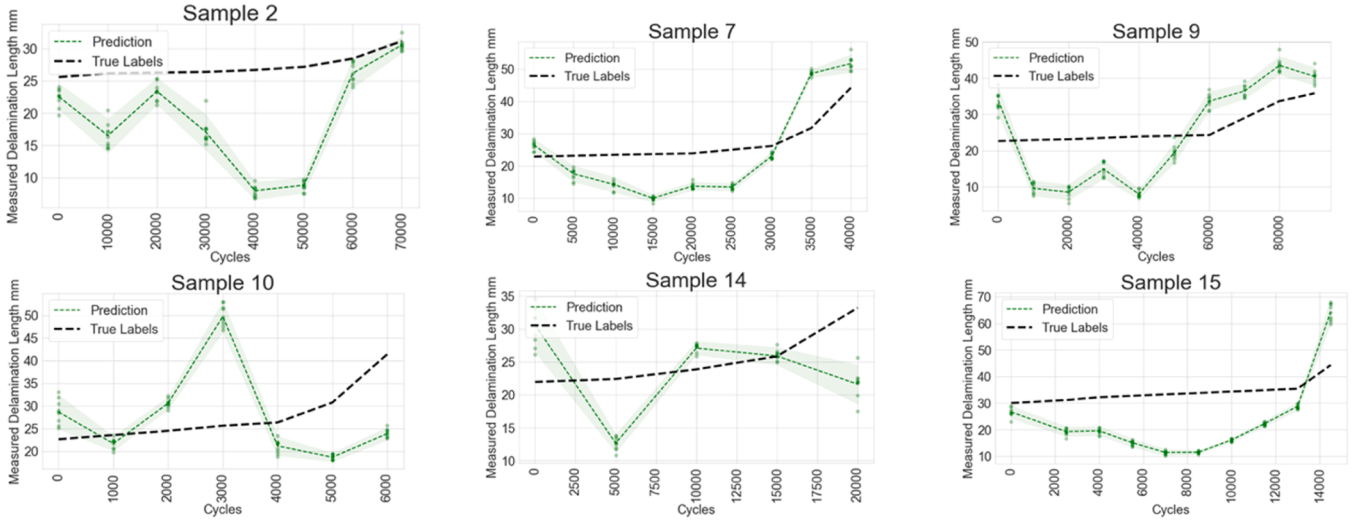

Fig. 12. Test results of delamination length predictions.

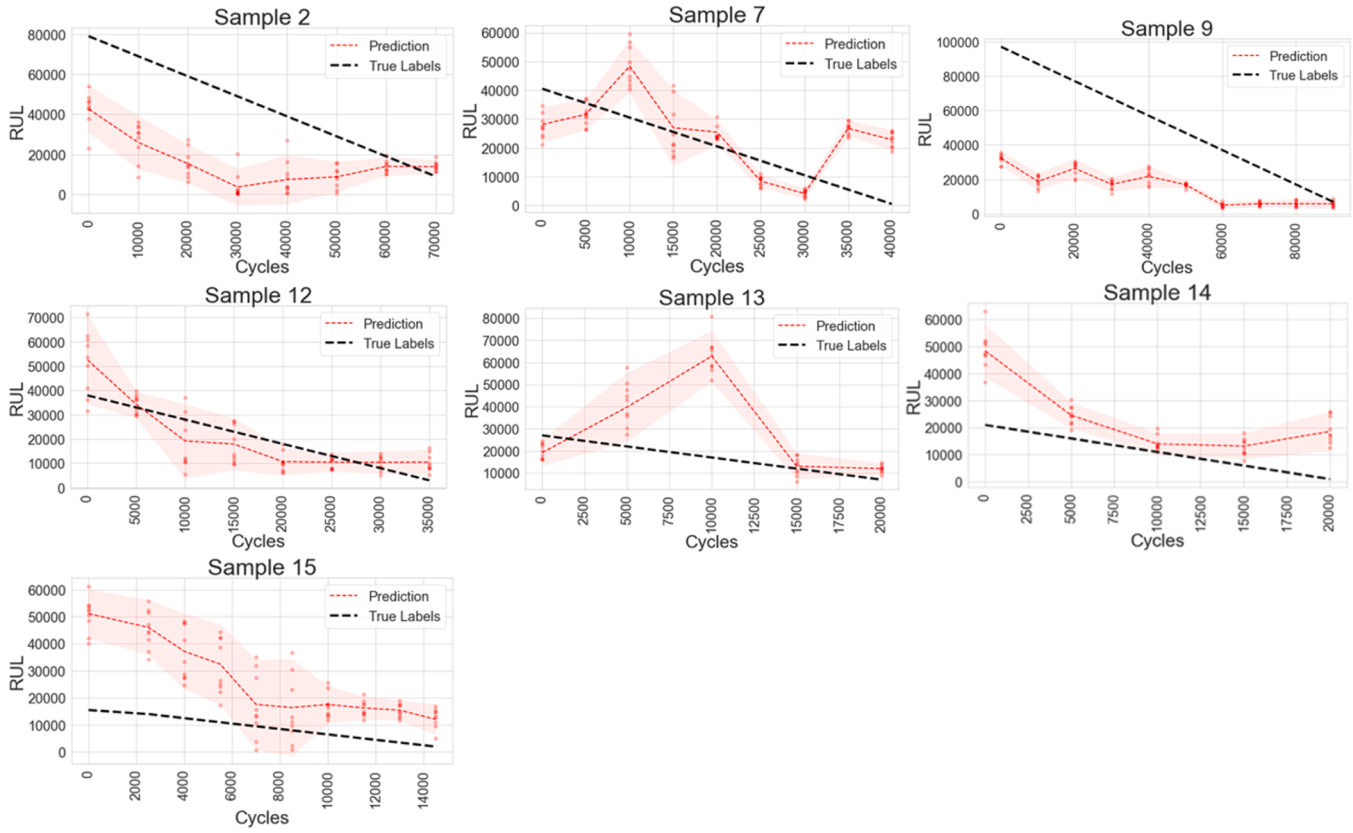

Fig. 13. Test results of RUL predictions.

poor convergence in earlier cycles, the model could converge in the last cycle differently than the results in Framework 1. In Fig. 13, the analysis suggests that the model exhibits a promising ability to approximate the monotonic behavior of RUL with relatively more robust performance observed in the predictions for Sample 7, Sample 12, and Sample 15. However, the relatively better accuracy of Sample 7 is not maintained after the 30000th cycle. Except for Sample 14 and Sample 7, RUL predictions are converging toward the final step. Sample 9 demonstrates an early prediction throughout the fatigue life of the sample. Sample 14 accurately predicts the RUL before the mid-life of the sample while still overestimating the final remaining time.

5.2.2. *Discussion*

In this section, damage propagation and RUL prognostics have been conducted within Framework 2, which ensembles samples from the dataset to create a more generic prediction model. For this purpose, samples with appropriate target characteristics are selected. While sub-type A requires a complete label set for the delamination length prediction, sub-type B aims for closer prognosability for the samples. As a result, six samples are assigned for type A, samples with numbers 2, 7, 9, 10, 14, and 15, and type B is trained and tested with Samples 2, 7, 9, 12, 13, 14, and 15 interchangeable for LOOCV folds.

It is observed for the RUL prediction that the distribution of the targets plays an important role in making efficient predictions, which refers to the overall prognosability of the training set. In the case of Sample 14 and Sample 15, their first cycle predictions are very high compared to the other samples in the dataset, which are the samples with a lower EoL. Once they are excluded from the training, the model's capability to predict lower values in the initial RUL step becomes less accurate.

In addition to model-based constraints, the DIs in the input data that play a significant role in the performance and can be the origin of less effective testing results. The possible noise and errors in acquired GW signals can be transferred to DI extraction, which may limit the model's learning capability. This effect might be mitigated in some ways, such as training the model with the raw signal in a supervised manner to eliminate DI extraction-based errors. However, adopting such an approach necessitates using more complex and deep learning architectures, which could decrease the explainability of the model. Another approach could involve increasing the number of samples in the dataset to encompass a broader range of damage and EoL scenarios. This would enhance the generalization capability of the model. On the other hand, creating such a dataset is highly challenging and resource-intensive, requiring significant experimental effort. Consequently, despite the constraints and the limited number of samples in the dataset, the results show promise in providing efficient and interpretable data- driven RUL and progressive damage prognostics.

6. Conclusion

This study presents a novel methodology to address RUL and delamination growth prognostic based on GW- SHM for CFRP samples subject to compressive fatigue loading after impact. Considering the proposed methodology, two main challenges have been aimed to be answered. To reveal the delamination state together with EoL of structure that possibly pave the way for reliable efficient RUL prognostic framework for the composite structures the prediction of delamination growth until a threshold level is included in a RUL prognostic framework to improve the reliability and effectiveness of the RUL prognosis. By adapting GW-DIs within a DNN- based regression model, a robust prognostic methodology is achieved, which enhances the explainability of RUL predictions, providing insights into the progression of delamination. Secondly, two frameworks are adapted to investigate various aspects of prognostics, one in an individual sample domain to reveal path dependency in RUL and delamination length prognosis and the second in an ensembled dataset domain proposing a more generic model

for RUL and delamination growth prediction.

In the domain of one sample-based analysis, results reveal that the actuator-sensor paths that demonstrate optimal performance in RUL prediction do not consistently coincide with those more sensitive to delamination. However, based on the results, the paths that indicate the highest accuracy for delamination growth prediction also tend to perform well for RUL prognostic. This may indicate for these samples that the corresponding GW- DIs might be more representative of the overall structural health state and perform better in the RUL prediction of the sample. Although the study notes variations in the sensitivity of different actuator-sensor paths to damage, it ultimately demonstrates the positive correlation between paths and their predictive capability in RUL and delaminations state.

As the second approach, the dataset is created with samples subjected to varied stress levels during their fatigue life, and the models account for multiple scenarios that have been achieved separately for RUL and delamination growth prognostic. Model performance for delamination and RUL predictions exhibit promising capability in capturing both targets through given GW-DIs. Furthermore, developing ensemble dataset-based DNN model demonstrate the methodology's robustness and adaptability across different stress scenarios and structural conditions.

Future work may focus on expanding the diversity and complexity of the dataset, incorporating real-world operational conditions, and exploring the potential of emerging deep-learning architectures for even more accurate and robust prognostic models. Extending this methodology to other composite materials and damage mechanisms could broaden its applicability, contributing to the need for effective prognostics that ensure the integrity and longevity of critical structures in a safe life.

CRediT authorship contribution statement

Ferda C. Gül: Conceptualization, Formal analysis, Methodology, Writing – original draft. **Morteza Moradi:** Conceptualization, Methodology, Writing – review & editing. **Dimitrios Zarouchas:** Conceptualization, Methodology, Supervision, Writing – review & editing.

Declaration of competing interest

The authors declare the following financial interests/personal relationships which may be considered as potential competing interests:

Ferda Cansu Gul reports financial support was provided by European Union. If there are other authors, they declare that they have no known competing financial interests or personal relationships that could have appeared to influence the work reported in this paper.

Acknowledgment

This project has received funding from the European Union's Horizon 2020 research and innovation programme under the Marie Sklodowska-Curie Grant No. 860104 "Guided Waves for Structural Health Monitoring".

Data availability

Data will be made available on request.

References

[1] M. Sadighi, R. Alderliesten, Impact fatigue, multiple and repeated low-velocity impacts on FRP composites: a review, Compos. Struct. 297 (2022), https://doi.org/10.1016/j.compstruct.2022.115962.

[2] J. Zhang, L. Zhao, M. Li, Y. Chen, Compressive fatigue behavior of low velocity impacted and quasi-static indented CFRP laminates, Compos. Struct. 133 (2015) 1009–1015, https://doi.org/10.1016/j.compstruct.2015.08.046.

[3] B. Yang, Y. Chen, J. Lee, K. Fu, Y. Li, In-plane compression response of woven CFRP composite after low-velocity impact: modelling and experiment, Thin Walled Struct. 158 (2021), https://doi.org/10.1016/j.tws.2020.107186.

[4] European Union Aviation Safety Agency, Annex to ED Decision 2022/001/R, General Acceptable Means of Compliance for Airworthiness of Products, Parts and Appliances (AMC-20). Amendment 23, 2022.

[5] M.R. Wisnom, The role of delamination in failure of fibre-reinforced composites, Philos. Trans. R. Soc. A Math. Phys. Eng. Sci. 370 (1965) 1850–1870, https://doi.org/10.1098/rsta.2011.0441. Apr. 2012.

[6] J.A. Pascoe, Slow-growth damage tolerance for fatigue after impact in FRP composites: why current research won't get us there, Theor. Appl. Fract. Mech. 116 (2021), https://doi.org/10.1016/j.tafmec.2021.103127.

[7] D. Biagini, J.A. Pascoe, R. Alderliesten, Investigating apparent plateau phases in fatigue after impact damage growth in CFRP with ultrasound scan and acoustic emissions, Int. J. Fatigue 177 (2023), https://doi.org/10.1016/j.ijfatigue.2023.107957.

[8] M.N. Saleh, H.M. El-Dessouky, M. Saeedifar, S.T. De Freitas, R.J. Scaife, D. Zarouchas, Compression after multiple low velocity impacts of NCF, 2D and 3D woven composites, Compos. Part A Appl. Sci. Manuf. 125 (2019), https://doi.org/10.1016/j.compositesa.2019.105576.

[9] S. Sanchez-Saez, E. Barbero, R. Zaera, C. Navarro, Compression after impact of thin composite laminates, Compos. Sci. Technol. 65 (13) (2005) 1911–1919, https://doi.org/10.1016/j.compscitech.2005.04.009.

[10] B. Ostré, C. Bouvet, C. Minot, J. Aboissière, Experimental analysis of CFRP laminates subjected to compression after edge impact, Compos. Struct. 152 (2016) 767–778, https://doi.org/10.1016/j.compstruct.2016.05.068.

[11] A. Güemes, A. Fernandez-Lopez, A.R. Pozo, J. Sierra-Pérez, Structural Health Monitoring for advanced composite structures: a review, J. Compos. Sci. 4 (1) (2020), https://doi.org/10.3390/jcs4010013. MDPI AG.

[12] V. Giurgiutiu, Structural Health Monitoring (SHM) of aerospace composites. Polymer Composites in the Aerospace Industry, Elsevier, 2019, pp. 491–558, https://doi.org/10.1016/B978-0-08-102679-3.00017-4.

[13] S. Sankararaman, K. Goebel, Uncertainty in prognostics and systems health management, Intl. J. Prognostics Health Mgmt 6 (2015), https://doi.org/10.36001/ijphm.2015.v6i4.2319.

[14] T. Loutas, N. Eleftheroglou, D. Zarouchas, A data-driven probabilistic framework towards the *in-situ* prognostics of fatigue life of composites based on acoustic emission data, Compos. Struct. 161 (2017) 522–529, https://doi.org/10.1016/j.compstruct.2016.10.109.

[15] G. Galanopoulos, N. Eleftheroglou, D. Milanoski, A. Broer, D. Zarouchas, T. Loutas, A novel strain-based health indicator for the Remaining Useful Life estimation of degrading composite structures, Compos. Struct. 306 (2023), https://doi.org/10.1016/j.compstruct.2022.116579.

[16] P. Cawley, M.J.S. Lowe, D.N. Alleyne, B. Pavlakovic, Practical long range guided wave testing: applications to pipes and rail, Mater. Eval. 61 (1) (2003).

[17] Z. Su, L. Ye, Y. Lu, Guided Lamb waves for identification of damage in composite structures: a review, J. Sound Vib. 295 (3–5) (2006) 753–780, https://doi.org/10.1016/j.jsv.2006.01.020.

[18] V. Janapati, F. Kopsaftopoulos, F. Li, S.J. Lee, F.K. Chang, Damage detection sensitivity characterization of acousto-ultrasound-based Structural Health Monitoring techniques, Struct. Health Monit. 15 (2) (2016) 143–161, https://doi.org/10.1177/1475921715627490.

[19] H. Liu, S. Liu, Z. Liu, N. Mrad, A.S. Milani, Data-driven approaches for characterization of delamination damage in composite materials, IEEE Trans. Ind. Electron. 68 (3) (2021) 2532–2542, https://doi.org/10.1109/TIE.2020.2973877.

[20] V. Giurgiutiu, Lamb wave generation with piezoelectric wafer active sensors for structural health monitoring. Proceedings of SPIE - The International Society for Optical Engineering 5056, 2003. 10.1117/12.483492.

[21] J.B. Ihn, F.K. Chang, Pitch-catch active sensing methods in Structural Health Monitoring for aircraft structures, Struct. Health Monit. 7 (1) (2008) 5–19, https://doi.org/10.1177/1475921707081979.

[22] C.M. Yeum, H. Sohn, J.B. Ihn, H.J. Lim, Instantaneous delamination detection in a composite plate using a dual piezoelectric transducer network, Compos. Struct. 94 (12) (2012) 3490–3499, https://doi.org/10.1016/j.compstruct.2012.06.003.

[23] C. Larrosa, K. Lonkar, F.K. Chang, *In situ* damage classification for composite laminates using Gaussian discriminant analysis, Struct. Health Monit. 13 (2) (2014) 190–204, https://doi.org/10.1177/1475921713517288.

[24] H. Liu, S. Liu, Z. Liu, N. Mrad, A.S. Milani, Data-driven approaches for characterization of delamination damage in composite materials, IEEE Trans. Ind. Electron. 68 (3) (2021) 2532–2542, https://doi.org/10.1109/TIE.2020.2973877.

[25] A. Saxena, K.F. Goebel, C.C. Larrosa, V. Janapati, S. Roy, F.-K. Chang, Accelerated aging experiments for prognostics of damage growth in compositeMaterials. ARC-E-DAA-TN3788, 2011.

[26] A.R. Diogo, B. Moreira, C.A.J. Gouveia, J.M.R.S. Tavares, A review of signal processing techniques for ultrasonic guided wave testing, Metals 12 (6) (2022), https://doi.org/10.3390/met12060936 (Basel).

[27] M. Rachid, A. Houda, B. Drissi Taoufiq, N. Benayad, Z. Soumaya, Post treatment of guided wave by using wavelet transform in the presence of a defect on surface, Intl. J. Adv. Com. Sci. Appl. 10 (7) (2019), https://doi.org/10.14569/IJACSA.2019.0100741.

[28] M. Rautela, J. Senthilnath, E. Monaco, S. Gopalakrishnan, Delamination prediction in composite panels using unsupervised-feature learning methods with wavelet-enhanced guided wave representations, Compos. Struct. 291 (2022), https://doi.org/10.1016/j.compstruct.2022.115579.

[29] X.S. Si, W. Wang, C.H. Hu, D.H. Zhou, Remaining Useful Life estimation - A review on the statistical data driven approaches, Eur. J. Oper. Res. 213 (1) (2011) 1–14, https://doi.org/10.1016/j.ejor.2010.11.018. Elsevier B.V.
[30] S. Ullah, A.A. Ijjeh, P. Kudela, Deep learning approach for delamination identification using animation of Lamb waves, Eng. Appl. Artif. Intell. 117 (2023), https://doi.org/10.1016/j.engappai.2022.105520.
[31] O. Fink, Q. Wang, M. Svensén, P. Dersin, W.J. Lee, M. Ducoffe, Potential, challenges and future directions for deep learning in prognostics and health management applications, Eng. Appl. Artif. Intell. 92 (2020), https://doi.org/10.1016/j.engappai.2020.103678.
[32] M. Moradi, F.C. Gul, D. Zarouchas, A novel machine learning model to design historical-independent health indicators for composite structures, Compos. B Eng. 275 (2024), https://doi.org/10.1016/j.compositesb.2024.111328.
[33] M. Moradi, A. Broer, J. Chiachío, R. Benedictus, T.H. Loutas, D. Zarouchas, Intelligent health indicator construction for prognostics of composite structures utilizing a semi-supervised deep neural network and SHM data, Eng. Appl. Artif. Intell. 117 (2023), https://doi.org/10.1016/j.engappai.2022.105502.
[34] X. Li, et al., Interpretable deep learning: interpretation, interpretability, trustworthiness, and beyond, Knowl. Inf. Syst. 64 (12) (2022) 3197–3234, https://doi.org/10.1007/s10115-022-01756-8.
[35] S. Haykin. Neural networks: a comprehensive foundation, Prentice Hall PTR, 1998. https://doi.org/10.1016/0967-0661(95)90080-2.
[36] M. El Mountassir, S. Yaacoubi, S. Dellagi, M. Sfar, M. Aouini, An ultrasonic guided waves based prognostic approach for predictive maintenance: experimental study cases, Mech. Syst. Signal. Process. 190 (2023) 110135, https://doi.org/10.1016/j.ymssp.2023.110135.
[37] S. Mishra, O.A. Vanli, Remaining useful life estimation with lamb-wave sensors based on wiener process and principal components regression, J. Nondestruct. Eval. 35 (1) (2016) 1–13, https://doi.org/10.1007/s10921-015-0328-2.
[38] Compass ASTM D7137 D7137M-17. Standard test method for compressive residual strength properties of damaged polymer matrix composite plates, 10.1520/D7137_D7137M-17.
[39] M. Barski, P. Pająk, Determination of dispersion curves for composite materials with the use of stiffness matrix method, Acta Mech. Autom. 11 (2) (2017) 121–128, https://doi.org/10.1515/ama-2017-0019.
[40] R. Soleimanpour, C.T. Ng, Scattering analysis of nonlinear Lamb waves at delaminations in composite laminates, JVC J. Vib. Control 28 (11–12) (2022) 1311–1323, https://doi.org/10.1177/1077546321990145.
[41] R. Gorgin, Y. Luo, Z. Wu, Environmental and operational conditions effects on Lamb wave based Structural Health Monitoring systems: a review, Ultrasonics 105 (2020), https://doi.org/10.1016/j.ultras.2020.106114.
[42] L. Yu, G. Santoni-Bottai, B. Xu, W. Liu, V. Giurgiutiu, Piezoelectric wafer active sensors for *in situ* ultrasonic-guided wave SHM, Fatigue Fract. Eng. Mater. Struct. 31 (8) (2008) 611–628, https://doi.org/10.1111/j.1460-2695.2008.01256.x.
[43] B. Zima, M. Rucka, Application of wavelet transform in analysis of guided wave propagation signals for damage detection in a steel plate, Diagnostyka 16 (2) (2015).
[44] A. Grossmann, J. Morlet, Decomposition of Hardy functions into square integrable wavelets of constant shape, SIAM J. Math. Anal. 15 (1984), https://doi.org/10.1137/0515056.
[45] H. Chen, M.J. Zuo, X. Wang, M.R. Hoseini, An adaptive Morlet wavelet filter for time-of-flight estimation in ultrasonic damage assessment, Measurement 43 (4) (2010) 570–585, https://doi.org/10.1016/j.measurement.2010.01.001 (Lond).
[46] X. Glorot, A. Bordes, and Y. Bengio, Deep sparse rectifier networks, Proceedings of the 14th International Conference on Artificial Intelligence and Statistics (AISTATS), 2011, pp. 315-323.
[47] D.P. Kingma and J.L. Ba, Adam, A method for stochastic optimization, 3rd International Conference on Learning Representations (ICLR), 2015, Conference Track Proceedings, 2015.
[48] N. Srivastava, G. Hinton, A. Krizhevsky, I. Sutskever, R. Salakhutdinov, Dropout: A simple way to prevent neural networks from overfitting, J. Mach. Learn. Res. 15 (2014), https://doi.org/10.5555/3045390.3045400.
[49] M. Despotovic, V. Nedic, D. Despotovic, S. Cvetanovic, Evaluation of empirical models for predicting monthly mean horizontal diffuse solar radiation, Renew. Sustain. Energy Rev. 56 (2016) 246–260, https://doi.org/10.1016/j.rser.2015.11.058. Elsevier Ltd.